Experimental Facility Development Toward Sound-Excitation Effects on Forced Convection Heat Transfer

C. Selcan,* B. Cukurel,† and J. Shashank‡
Technion–Israel Institute of Technology, 32000 Haifa, Israel

DOI: 10.2514/1.T4607

In light of the background in periodic boundary-layer forcing as employed for flow control applications, the present work discusses the role of standing acoustic waves toward convective heat transfer modification in a turbulent straight channel flow. To this end, a dedicated low-speed wind-tunnel facility is designed, analyzed, and built, and it is specifically geared toward comprehensive investigation of sound-excited heat transfer for different aerodynamic and acoustic boundary conditions. To identify frequency ranges conducive toward exciting acoustic resonances, both in the transverse and longitudinal directions, a detailed numerical analysis of the acoustic resonance behavior is carried out. Resulting mode patterns and arising pressure nodes and antinodes are discussed in detail. On selected transverse and complex coupled modes, experimental surface temperature measurements are carried out by steady wideband liquid crystal thermometry. Findings indicate that, depending on the matched eigenfrequency and standing wave pattern, a slight elevation or reduction of heat transfer (locally and globally) is possible, whereas no change is observed for the pure traveling wave forcing. Although the acoustically induced changes are small in magnitude, the dependence on the excitation frequency is clearly quantifiable beyond the measurement error.

Nomenclature

a	=	air speed of sound, m/s
C_p	=	specific heat capacity, J/Kg K
Ec	=	Eckert number
H	=	hue-angle attribute
H_i	=	bell-mouth entry height, m
H_o	=	bell-mouth exit height, m
h	=	heat transfer coefficient, $W/m^2 \cdot K$
k	=	air thermal conductivity, $W/m \cdot K$
L	=	problem characteristic length scale, m
Nu	=	Nusselt number
Pr	=	Prandtl number
Re	=	Reynolds number
T	=	temperature, K
t	=	time, s
U_e	=	external flow velocity, m/s
u, v	=	velocity, m/s
X_I	=	bell-mouth length, m
x	=	axial direction, m
y	=	normal direction, m
δ	=	displacement thickness, m
δ_S	=	Stokes layer thickness, m
ϑ	=	momentum thickness, m
λ	=	sound wavelength, nm
ν	=	kinematic viscosity, m^2/s
ρ	=	density, kg/m^3
ω	=	acoustic sound frequency, Hz

Subscripts

0	=	steady
1	=	unsteady
∞	=	freestream

Received 10 October 2014; revision received 9 August 2015; accepted for publication 9 October 2015; published online 4 January 2016.

*Graduate Student, Turbomachinery and Heat Transfer Laboratory, Faculty of Aerospace Engineering, Technion City.

†Assistant Professor, Turbomachinery and Heat Transfer Laboratory, Faculty of Aerospace Engineering, Technion City.

‡Research Engineer, Turbomachinery and Heat Transfer Laboratory, Faculty of Aerospace Engineering, Technion City.

I. Introduction

IN THE field of aerodynamics, modification of bounded and unbounded shear flows by the deliberate introduction of small-amplitude periodic disturbances has emerged as a well-established technique toward controlling a range of fluid dynamics problems, e.g., delay of boundary-layer separation, transition to turbulence, and control of turbulence quantities [1–3]. Perturbations are commonly imposed either by global (acoustic) or localized (synthetic jets, mechanical flaps, dielectric barrier discharges, etc.) means of forcing [4]. Historically, although numerous investigations examined the direct aerodynamic implication of periodic flow perturbation, the ensuing impact on the thermal boundary-layer development (thus convective heat transfer) received much less attention, even for flat-plate and rearward-facing step-type fundamental geometries. Pertinent literature on this problem is generally scarce and mostly uncorrelated.

Four potential mechanisms are inferred to govern periodically forced aerothermal boundary-layer flow: periodic flow reversal, triggered shear-flow instability, oscillation-induced turbulence, and steady streaming [5]. Periodic flow reversal becomes relevant only in high-amplitude pulsating flows [5]. Excitation of shear flow and stimulation of coherent structure dynamics are of importance in separating and reattaching flows [1]. The possibility of oscillation-induced, localized, and time-dependent transition is prominent, especially for quasi-laminar flow subjected to high forcing amplitudes [6]. For small-amplitude excitation of turbulent flow, as covered herein, the steady streaming effect is most relevant.

Toward establishing the basis of the current investigation's framework, the theoretical background on steady streaming, as induced by traveling and standing sound wave motion upon wall interaction, is discussed in detail.

Temporally oscillating flow is typically classified by the presence or absence of the mean flow component [7,8]. Although non-vanishing mean flow is evidently of higher relevance to the majority of engineering applications, classic analytical solutions to periodic boundary-layer motion consider the absence of a mean velocity component.

The simplest problem of flow unsteadiness is associated with a temporal change of the external flow velocity, typically characterized by a single harmonic oscillatory component of a traveling wave/Stokes oscillating (flat) plate problem [9]. For a harmonic oscillation of the freestream component, the problem's solution

$$u = U_0[\sin(2\pi\omega t) - \exp(-y/\sqrt{(2\nu/\omega)}) \cdot \sin(2\pi\omega t - y/\sqrt{(2\nu/\omega)})] \tag{1}$$

is composed of the inviscid and viscous boundary-layer responses. Thereby, the shear originates from the wall and propagates into the fluid by means of an exponentially damped traveling wave. The characteristic length scale associated with this attenuation process, $\delta_S \sim \sqrt{\nu/\omega}$, is known as the Stokes layer or viscous diffusion thickness. This thin near-wall region describes the retardation of acoustic wave-introduced flow motion in the boundary layer [10,11].

The two-dimensional Navier–Stokes equations can be written in the nondimensional form [8]

$$\frac{\partial u}{\partial t} + \frac{U_1}{\omega L} \cdot \left(u\frac{\partial u}{\partial x} + v\frac{\partial u}{\partial y}\right) = -\frac{\partial p}{\partial x} + \frac{\nu}{\omega L^2} \cdot \frac{\partial^2 u}{\partial x^2} + \frac{\partial^2 u}{\partial y^2} \tag{2}$$

where U_1 and $\omega = t_0^{-1}$ denote the characteristic velocity amplitude and the frequency scale, respectively; and y and v are scaled with respect to the Stokes layer thickness δ_S. Absent of mean flow, two characteristic similarity variables are formed:

$$\nu/(\omega L^2) = (\delta_s/L)^2 \tag{3}$$

$$\varepsilon = U_1/(\omega L) \tag{4}$$

with the former scaling diffusion in the wall normal direction with respect to the streamwise direction. For the case of $U_1/\omega L \gg \nu/\omega L^2$, the boundary-layer assumption holds $\partial^2/\partial y^2 \gg \partial^2/\partial x^2$ [7]. When writing the pressure gradient by the driving velocity at the boundary-layer edge U_e, Eq. (2) can be formulated as follows:

$$\frac{\partial u}{\partial t} - \frac{\partial^2 u}{\partial y^2} - \frac{\partial U_e}{\partial t} = \frac{U_1}{\omega L} \cdot \left(U_e\frac{\partial U_e}{\partial x} - u\frac{\partial u}{\partial x} - v\frac{\partial u}{\partial y}\right) \tag{5}$$

Evidently, the second nondimensional parameter ε scales the extent of characterizes the extent of streamwise convection with respect to the diffusion in the normal direction, characterizing the problem's nonlinearity. The high-frequency limiting case, assuming a small velocity fluctuation amplitude U_1 and high oscillation frequency ω [12]

$$U_1/(\omega L) \ll 1 \tag{6}$$

is apparent to render the problem linear by inducing vanishing convective terms in the first-order approximation [7].

This forms the basis of the second-order boundary-layer phenomenon known as steady streaming, where small-amplitude periodic freestream oscillations induce a steady velocity component in the near-wall region due to the nonlinear boundary-layer response. The mean velocity component is of finite magnitude at the Stokes layer edge:

$$u(x, \delta_S) = -3/4 \cdot U_1/\omega \cdot \mathrm{d}U_1/\mathrm{d}x \approx U_1^2/\omega L \tag{7}$$

The mechanism of Stokes layer formation also holds great significance to the nonvanishing mean boundary-layer flows [8]. In the case of low oscillation frequencies, the Stokes and steady boundary layers are of equal thickness, and thus significant to the wall near the flowfield [13]. Therefore, their interaction in the low-frequency case is fully coupled (Fig. 1a):

$$\omega \cdot \vartheta^2/\nu = \vartheta^2/\delta_S^2 = \mathcal{O}(1) \tag{8}$$

In contrast, for high-frequency oscillations, the Stokes layer is very thin compared to the steady boundary-layer momentum thickness ϑ, thus enabling independent treatment of both (Fig. 1b) [8,12]:

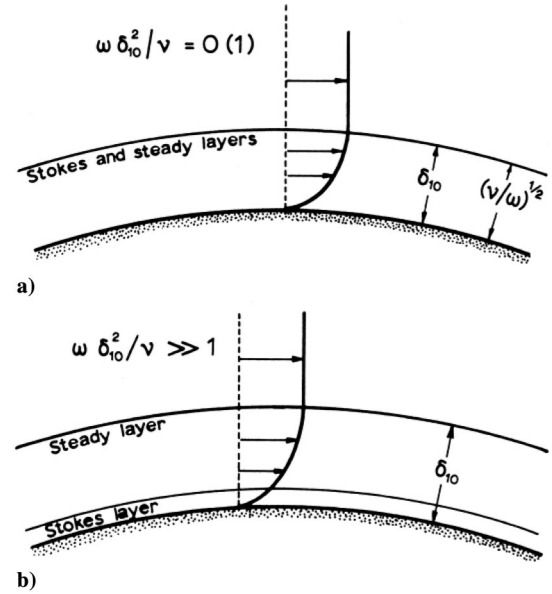

Fig. 1 Stokes and steady boundary layers [13].

$$\omega \cdot \vartheta^2/\nu = \vartheta^2/\delta_S^2 \gg 1 \tag{9}$$

Considering fluid flow along a nonadiabatic passage with acoustically coupled convection phenomena taking place, the aerothermal flowfield is seen to be determined by the following parameter space:

$$f(U_0, U_1, L, \omega, T_\infty, \Delta T, h, \rho, \nu, k, c_p) = 0 \tag{10}$$

denoting steady and fluctuating velocity scales, length scale, oscillation frequency, fluid temperature, temperature head, convective heat transfer coefficient, and thermophysical properties of air (density, kinematic viscosity, thermal conductivity, and specific heat capacity). The problem is thus described by seven characteristic nondimensional numbers:

$$f\left(\frac{\omega L}{U_1}, \frac{U_1}{U_0}, \frac{\Delta T}{T_\infty}, Re_0, Pr, Nu, Ec\right) = 0 \tag{11}$$

At low flow velocities and limited compressibility effects (for excitation $\lambda \gg L$), the Eckert number becomes negligible. In addition, for insignificant fluid property variation at small temperature differences, the Prandtl number and the relative bulk flow temperature $\Delta T/T_\infty$ can be omitted [14]. The problem of convective heat transfer in oscillatory flow is thus governed by

$$Nu = f\left(\frac{\omega L}{U_1}, \frac{U_1}{U_0}, Re_0\right) \tag{12}$$

where unsteadiness-induced flow phenomena are described by the frequency parameter and the velocity ratio.

The impact of sound excitation on natural convection heat transfer was comprehensively demonstrated by a broad range of studies [15–17]. Attributed to forcing-induced thermoacoustic streaming in a frequency range up to 5 kHz, notable heat transfer enhancement was reported; generally, effects became more pronounced with higher sound pressure levels (SPLs). In the ultrasound range (30 kHz), the significance of acoustic streaming and its effectiveness toward heat transfer enhancement was observed, highlighting the relevance of the longitudinal excitation-induced velocity component [18].

In contrast to natural convection, literature focusing on the acoustically excited forced convection heat transfer yielded conflicting results. Some studies reported notable augmentation of laminar and turbulent flow heat transfers [19–21]. Beyond a critical SPL excitation limit, the averaged heat transfer was found to be

increased by 40% for moderate mean flow Reynolds numbers, $Re \sim \mathcal{O}(10^5)$; however, no explicit frequency dependence was ascertained [21]. Similar results were observed for heat transfer from wires at much lower Reynolds numbers [22]. In contrast, other studies indicated a detrimental influence of sound excitation on heat transfer or no effect at all [23,24].

As traveling waves interact with boundaries, interference of the incident and reflected waves can give rise to a spatially stationary and temporally oscillating static pressure field. This resultant constructive interference is known as a standing wave, inducing pressure fluctuations and associated acoustic particle velocity fields, which exceed the incident wave amplitude.

Standing wave effects on forced convection heat transfer have been demonstrated, particularly for longitudinal resonance modes in turbulent flow, highlighting the importance of Reynolds numbers and standing wave patterns [25–27].

At low Reynolds numbers ($Re \leq 35{,}000$), locally elevated and reduced heat transfer regions were reported to coincide with the longitudinal velocity antinodes and nodes, respectively. On the contrary, higher Reynolds numbers switched the locations of maximum and minimum Nusselt numbers to the pressure antinodes and nodes [28]. Globally, the heat transfer was found to be unaffected by resonances at low Reynolds number, whereas high Reynolds numbers led to a reduction in global heat transfer [28]. Contradictory findings by other investigators indicated an overall increase in heat transfer, where the exerted influence of the longitudinal resonance conditions depended on the boundary-layer state, inducing augmentations as large as 50 and 20% in laminar and turbulent flows, respectively [29,30]. The authors who found heat transfer to increase both with rising SPL and resonance frequency ascribed excitation-induced effects to a thinning of the Stokes layer, which increased the near-wall flow gradients [30].

Besides the impact of longitudinal resonances, studies on combustion instability-driven pressure oscillations found heat transfer in a straight circular pipe to be notably increased by the presence of transverse modes, inducing tangential velocities normal to the main flow direction [31].

Considering the highly contradictory results associated with sound-excited forced convection heat transfer in the presence of acoustic resonance modes, absent of a predictive theory, practical exploitation of such effects is evidently impeded by the limited understanding of the underlying physical mechanisms. Owing to the complex and coupled aerothermal interactions present, a more comprehensive perspective can be attained via establishment of a dedicated experimental facility, contributing to the pool of efforts on the subject.

To this end, a versatile low-speed wind-tunnel facility, which can be equipped with various types of acoustic drivers, is designed in order to carry out experiments in a range of Reynolds numbers, sound pressure levels, and absolute/reduced forcing frequencies. The wind tunnel's acoustic resonance behavior is characterized in detail by means of a dedicated numerical eigenfrequency analysis. The experimental findings presented herein exemplify the effects of the less investigated transverse and coupled resonance modes on turbulent forced convection heat transfer.

To facilitate the expansion of the fundamental knowledgebase in sound wave/boundary-layer interaction, this paper strives toward disseminating the scientific background and anterior experimental design philosophy of a dedicated measurement campaign.

II. Methodology

A. Experimental Facility

1. *Test Section and Instrumentation*

The experimental wind-tunnel facility employed is operated by a centrifugal blower running in aspiration mode. To prevent transmission of the mechanical vibrations toward the test section, the wind tunnel is mechanically decoupled from the driving unit by a multiconvoluted bellow-type expansion joint. With its inherently low nonlinear spring constant, it is ideal for applications that require significant amounts of axial and lateral movements. Pressure fluctuations from the driving unit are damped by a settling chamber, equipped with two layers of taut metal, wire mesh structures with a uniform cell size of 1 mm and 40% area blockage ratio. The duct that forms the test and exhaust sections has a 20×20 cm cross section at a length of 4 m. Upstream, the air is sucked in through a bell-mouth inlet with a contraction area ratio of 25 : 1. On the low-speed end, the construction contains a 20-cm-thick honeycomb with a 1 cm cell size that creates a blockage ratio of 25%, accompanied by a metal screen (1 mm cell size and 40% area blockage ratio). These features minimize inflow swirl while diminishing spatial nonuniformities.

For setting the aerodynamic operating conditions along the channel, the bulk velocity is measured via a Paragon FE-1500-FX duct-mounted airflow measurement station, along with six T-type thermocouples exposed to freestream air at the test section inlet and outlet. The facility schematic can be found in Fig. 2.

The test section comprises 1.5-m-long Plexiglas walls that are supported by an aluminum frame. Thereby, optical access is enabled from three sides, where one sidewall serves as the investigation surface for heat transfer measurements. The static pressure distribution over the test channel is acquired by pressure taps located along the wall. The design of the test section features multifunction

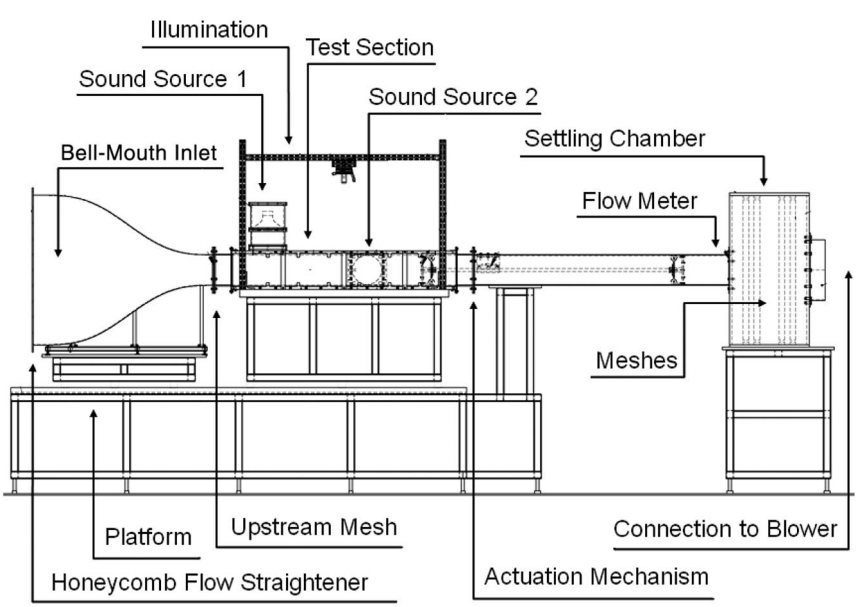

Fig. 2 Schematic of the experimental facility.

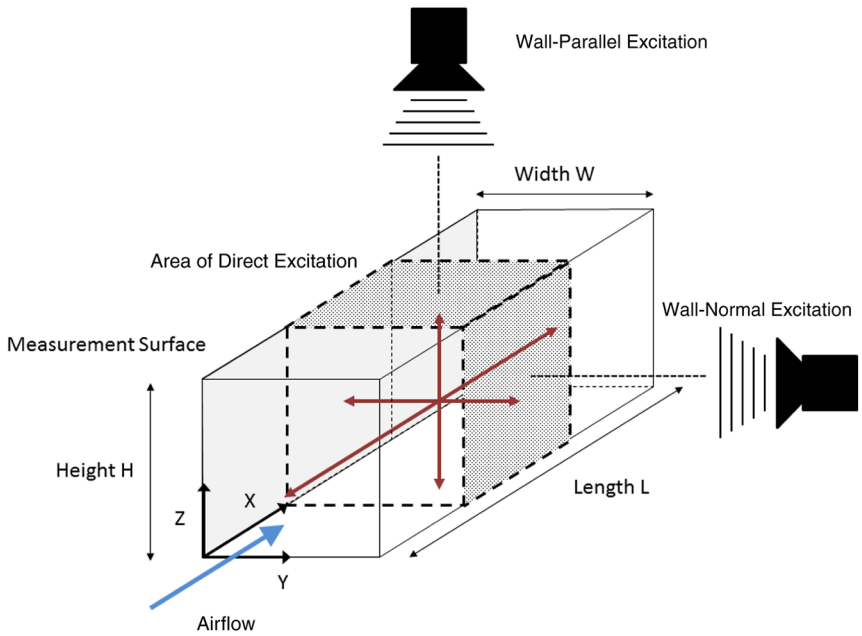

Fig. 3 Illustration of the experimental test section.

ports that grant maximum flexibility for attaching a range of acoustic drivers on the lateral and adjacent top walls, thereby allowing acoustic excitation of the measurement surface boundary layer in wall-normal and parallel directions (Fig. 3).

A Mackie DLM-8 loudspeaker is employed as the active audible frequency range excitation source (65–20 kHz), which is placed in a sealed casing on the observation sidewall. A squared, taut, fine, steel wire mesh (25 μm cell size), covering the entire 20 cm duct height, prevents perturbation of the channel flow. Acoustic boundary conditions are acquired by a high-sensitivity wide frequency range (4–70 kHz) pressure field condenser microphone (type G.R.A.S. 46BD) flush mounted to the heat transfer surface sidewall at the centerline. The signal is amplified with an Endevco Meggitt model 133 conditioner, followed by acquisition via a National Instruments 9205 module at 200 kS/s sampling rate, and subsequent fast Fourier transform spectral analysis.

At mean velocity values ranging from 5 to 50 m/s and channel hydraulic diameter-based Reynolds numbers of $5 \cdot (10^4\text{–}10^5)$, the facility is capable of reproducing conditions of the acoustic particle to mean velocity ratios $U_1/U_0 = 10^{-5} - 5 \cdot 10^{-2}$ and frequency parameters $\omega L/U_1 = 5 \cdot 10^2 - 2 \cdot 10^6$. Absent of forcing, the typical background SPL inside the test section throughout experiments is on the order of 80 dB for mean flow velocities of 10 m/s.

2. *Linear Actuation Mechanism*

To study the impact of longitudinal standing waves, the experimental setup is employed with two fine, steel wire meshes (25 μm cell size with 90% blockage ratio) that confine the upstream and downstream ends of the test section. The mesh structures modify the acoustic boundary conditions by partial wave reflection and encourage formation of a cuboid closed-duct cavity that mimics a resonance tube behavior [32]. To study the effect of varying frequency resonance modes, a LinMOT linear actuation mechanism is incorporated. Although the upstream mesh remains fixed, the translation of the downstream mesh allows adjusting the natural frequencies of the fluid column by varying the length of the test section.

Assuming a cuboid space of acoustically hard walls and length L, width W, and height H (Fig. 3), the resonance frequencies are estimated in a first approximation according to

$$f_{l,m,n} = a/2 \cdot \sqrt{(l/L)^2 + (m/W)^2 + (n/H)^2} \tag{13}$$

where $l, m, n = 0, 1, 2 \ldots$ denote the higher harmonics.

3. *Bell-Mouth Inlet*

To ensure flow conditioning at small acoustic to mean velocity ratios, the bell-mouth geometry was designed following the low-speed wind-tunnel guidelines of Bell and Mehta [33,34]. The design considerations include a thin boundary layer and flow uniformity, as well as avoidance of intermittent separation and ensuing unsteadiness.

Starting from the original proposed fifth-order polynomial that satisfies the suggested zero wall slope and curvature conditions at the inlet and outlet of the contraction, a modification of the profile by Brassard and Ferchichi [35] was considered:

$$h(\zeta) = ((-10\zeta^3 + 15\zeta^4 - 6\zeta^5) \cdot (H_R^{1/\alpha} - 1) + 1)^\alpha \tag{14}$$

where $\zeta = x/X_I$, $h = H(\zeta)/H_o$ and $H_R = H_i/H_o$.

Selected bell-mouth dimensions ($H_R = 5$ and $X_I/H_i = 1.2$) yield wall curvature radii proportional to the cross-section area and continuous surface transition toward the test section. A sinusoidal transformation exponent, $\alpha = \sin(\zeta \cdot \pi/2) + 0.01$, is chosen to further diminish the gradients at the inlet.

Bell-mouth performance was verified by a potential flow computation following Thwaites's boundary-layer solution [36]. Denoting a stable laminar boundary-layer velocity profile, the shape factor along the inlet varied between $H = 2.59$ and $H = 2.13$ [7]. At the outlet, the shape factor equals $H = 2.594$; the displacement and momentum thicknesses are $\delta = (4.06 - 12.83) \cdot 10^{-4}$ m and $\theta = (1.56 - 4.95) \cdot 10^{-4}$ m for freestream velocities of 5–50 m/s. The equivalent flat-plate entry length associated with the bell-mouth inlet, from the Blasius boundary-layer solution $\delta = 5x/Re_x$, is of a 2 cm order.

B. Measurement Methodology

1. *Liquid Crystal Thermometry*

The measurement of time-averaged convective heat transfer is conducted by means of wideband liquid crystal thermometry at a steady state. This allows optical acquisition of high-resolution spatial distributions of the surface temperature and heat transfer coefficient. Cholesteric microencapsulated thermochromic liquid crystals (TLCs) (type R35C20W by Hallcrest, Inc.) are employed. For the active temperature interval of 35–55°C, the color play is within the bandwidth of 400–700 nm. A spatially uniform constant heat flux thermal boundary condition is implemented by a 25-μm-thick Inconel foil, which is attached to the vertical heat transfer measurement surface. Connected to a dc power supply, it provides heating of

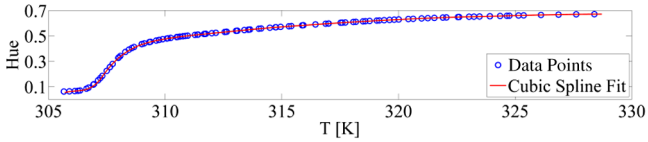

Fig. 4 Hue-temperature calibration curve.

the test section via joule heating; the imposed surface heat flux q is calculated from the supplied voltage and current, $q = V \cdot I$.

Inconel is chosen due to a high electrical resistivity at a low-temperature coefficient of resistance, which is ideal for providing high power in a small area in a wide temperature range. Its thermoelectrical properties facilitate uniform-distribution isocurrent lines, thereby providing constant surface heat flux.

2. *Optical Observation and Illumination*

For optimal TLC color play brilliance and contrast, the thermochromic liquid crystals are deposited on a uniform underlying layer of matte black paint, which exhibits a nondazzling surface due to diffuse reflection. The test surface TLC response is observed via a Nikon D300S digital camera, placed at a 20 deg observation angle from the channel axis. A camera offaxis illumination configuration is used, ensuring minimum surface reflections and shadows, as well as overcoming issues of nonuniformity.

Illumination is provided by OSRAM type T8 L 36 W fluorescent lights mounted above the principal axis, irradiating at a vertical 1 m distance to the TLC surface (Fig. 2). The entire test section and observation camera are covered by thick black cloth to prevent spurious background illumination sources.

3. *Hue Calibration and Data Reduction*

During data acquisition, high-resolution images of the test surface are captured in the red, green, and blue tristimulus value (known as RGB) color space of the camera. To reduce a possible angular dependency due to the camera-lighting offaxis arrangement, a background subtraction routine is used. RGB values of the unheated and inactivated TLC surface (background image) are sampled at the beginning of an experiment and subsequently subtracted from every measurement image. The effectiveness of this methodology has been previously demonstrated [37].

For local temperature acquisition, the RGB color is transformed into the hue, saturation, and intensity domain space; the hue-angle color quantity

$$H = 1/2\pi \cdot \tan^{-1}[\sqrt{3} \cdot (G - B)/(2R - G - B)] \tag{15}$$

can be uniquely correlated to temperature by a monotonously increasing, single valued, and continuous function. This enables the unambiguous calculation of a numerically averaged local surface temperature from the camera-recorded TLC response.

The hue-temperature calibration curve (Fig. 4) is established by an in situ calibration at natural convection using four T-type surface thermocouples located at the downstream end of the test plate. Arranged in a cross-shaped configuration and enclosing a small square TLC-coated area (1×1 cm), the hue-angle value of the exposed TLC area is acquired and correlated with the averaged thermocouple readings. The successively imposed temperature levels span the entire TLC color play bandwidth. Discrete data are fitted by a twice-differentiable monotonically increasing 20 kt cubic spline. Details of the TLC thermometry technique and the calibration procedure are given in [37].

4. *Image Processing*

Due to the inclined observation path, sampled images are subject to significant perspective distortions. This necessitates mapping and projection of each region of the image separately onto a single plane via independent bicubic transformation (Fig. 5). Accordingly, due to the optical path, the magnification factor varies along the test plane; as an overall indicator, the averaged mean scale factor is calculated to be 12 pixels/mm.

Finally, after using the calibration curves and converting acquired hue-angle distributions to the desired maps of surface temperatures, the raw temperature data are subjected to a series of filters. Initially, a median filtering methodology is used; this is typical for applications where the goal is to simultaneously reduce peek noise and preserve edges. In the following, the resulting temperature distribution is passed through a Gaussian low-pass filter to smooth out the local superficially high gradients of temperature. As a result, the final spatially averaged absolute error caused by postprocessing is approximately 0.15 K, and it varies slightly along the investigation domain due to out of focus effects.

5. *Enhancement Factor Calculation*

The local convective heat transfer coefficient is calculated from the imposed Inconel heat flux, the TLC-acquired surface temperature, and the bulk temperature along the channel axis:

$$h(x, y) = q/(T(x, y) - T_\infty(x)) \tag{16}$$

Subsequently, it is represented as a Nusselt number: the local characteristic length x measured in reference to the upstream mesh at the flat-plate section inlet:

$$Nu_x(x, y) = h(x, y) \cdot x/k_{\text{air}} \tag{17}$$

Convective heat transfer modification due to acoustic excitation is quantified by the local enhancement factor (EF), contrasting Nusselt numbers Nu_x, and the absence and presence of forcing:

$$EF = Nu_{\text{excited}}/Nu_{\text{unexcited}} \tag{18}$$

C. Uncertainty Analysis

The measurement uncertainty is estimated according to the single sample method proposed by Kline and McClintock [38].

Toward isolating the ramifications of a distinct phenomenon, the readings at desired conditions are typically contrasted to a reference/baseline case. Under these circumstances, the absolute quantities becomes less significant. Characterizing the precision of the dimension, the measurement repeatability is of relevance. In this case, the precision error of the wall temperature measurement is related to the hue-angle contribution of the fixed broadband image noise, which is computed to be on the order of ± 0.25 K. Moreover, under typical experimental conditions, there exist bulk fluid temperature variations within ± 0.2 K. Therefore, the resultant wall temperature repeatability is within ± 0.3 K. The propagation of this precision error to the heat transfer coefficient and the Nusselt number contribute to deviations up to $\pm 1.5\%$. Since the enhancement factor

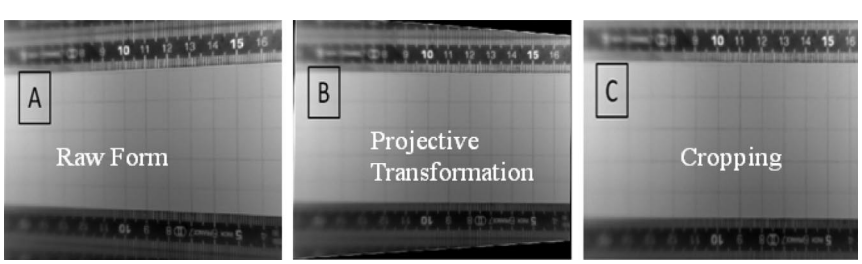

Fig. 5 Correction steps of perspective distortions.

Table 1 Numerical simulation boundary conditions

Parameter	Value
Wall enclosure	Acoustically hard (rigid) wall
Inlet	Plane wave radiation Incident pressure wave (1 Pa)
Outlet	Plane wave radiation

Table 2 Porous surface modeling parameters

	Interior perforated plates		
Characteristics	Mesh	Honeycomb	Screens
Area porosity σ	0.1	0.75	0.6
Hole diameter d_h, m	$25 \cdot 10^{-6}$	0.010	0.001
Plate thickness t_p, m	0.0001	0.200	0.0007
End correction δ_h	$0.25d_h$	$0.25d_h$	$0.25d_h$
Flow resistance θ_f	— —	— —	— —

is, by definition, a relative quantity, the total uncertainty associated is also within ±1.5% in the 95% confidence interval.

The overall uncertainty in the wall temperature is determined by the combination of accuracy- and precision-related errors. The contributors to the accuracy of the wall temperature measurement include uncertainty of the thermocouple reading (±0.35 K), the liquid crystal angular dependency (±0.3 K), and deviation from the hue-temperature curve fit formulation (±0.2 K). The resultant bias error is within ±0.5 K. This combined (accuracy and precision) wall temperature uncertainty is ±0.56 K.

The major contributors to the surface heat flux uncertainty (±2.4%) are the back face conduction loss (up to ±2%) and the Inconel area uncertainty (±1.3%). Along with the uncertainty of the convective heat transfer coefficient (±3.5%), hydraulic diameter measurement (±0.56%), and air thermal conductivity (±0.15%), the resulting combined Nusselt number uncertainty is estimated as ±4%.

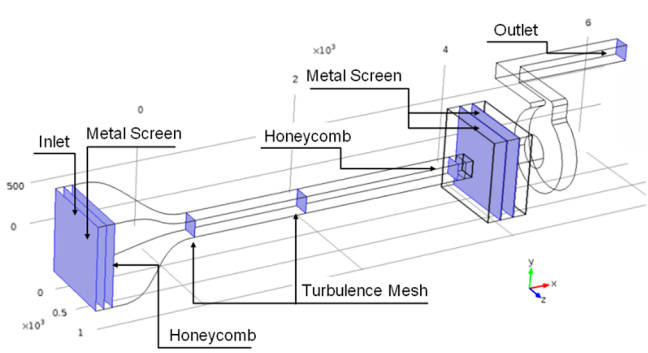

Fig. 6 Computational domain boundary conditions.

III. Numerical Simulation Approach

To accurately predict complex modal characteristics and natural frequencies of the experimental test rig, a numerical simulation is carried out by COMSOL Multiphysics®. By assuming rigid boundary conditions for the passage enclosure and considering a low mean flow Mach number ($Ma \ll 0.1$), the numerical domain is modeled by the acoustic module, where sound-structural and aeroacoustic coupling is neglected. The finite element model (FEM)-modeled three-dimensional geometry includes every air cavity component of the test facility: the upstream bell-mouth inlet, the squared test section duct, and the downstream settling chamber, as well as the compressor plenum and air outlet duct.

An unstructured mesh of 668,100 second-order Lagrange tetrahedral elements (971,000 degrees of freedom) is used to solve the Helmholtz equation [Eq. (19)] in the frequency domain. Viscous dissipation and thermal effects are not modeled, and the loss term in Eq. (19) is thus neglected; the properties of air are assumed constant. For appropriate resolution of the sound waves, the mesh element size (maximum of 40 mm) is set to be less than one-fifth of the minimum wavelength of interest:

$$\nabla \cdot \left(-\frac{1}{\rho_0}(\nabla p - q) \right) - \frac{\omega^2 p}{\rho_0 c^2} = Q \tag{19}$$

The simulation is conducted using the boundary conditions listed in Tables 1 and 2: although rigid walls (sound hard boundary condition) are assumed for the enclosure, plane wave radiation is set at the inlet and outlet sections (Fig. 6). Honeycomb turbulence meshes and screen inserts are modeled as interior perforated plates: as the Mach number is small ($Ma \ll 0.1$), the convective effects and flow resistance θ_f across the plate boundaries are omitted. Acoustic transfer impedances Z are calculated according to the model expression [39]

$$\frac{Z}{\rho_c c_c} = \left(\frac{1}{\sigma} \sqrt{\frac{8\,\mu k_{\mathrm{eq}}}{\rho_c c_c}} \left(1 + \frac{t_p}{d_h} \right) + \theta_f \right) + i \frac{k_{\mathrm{eq}}}{\sigma} (t_\rho + \delta_h) \tag{20}$$

A two-step frequency domain analysis approach is used. Initially, the integral transmission loss (TL) is studied over the entire domain for a unit excitation incident pressure wave (1 Pa) at the inlet [Eq. (21)]. This facilitates identification of the prominent natural frequencies to be encountered during wind-tunnel operation:

$$\mathrm{TL} = 10 \cdot \log\left(\frac{w_{\mathrm{out}}}{w_{\mathrm{in}}} \right) = 10 \cdot \log\left(\frac{\frac{p^2}{2\rho c} dS|_{\mathrm{out}}}{\frac{p^2}{2\rho c} dS|_{\mathrm{in}}} \right) \tag{21}$$

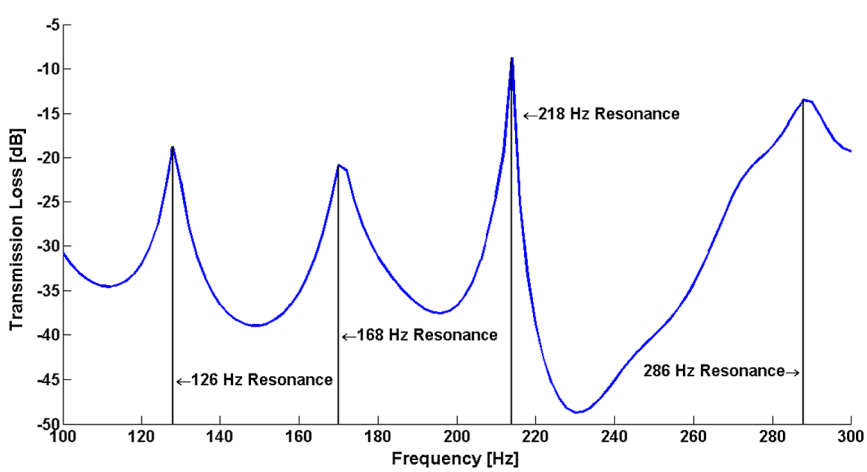

Fig. 7 Wind-tunnel transmission loss.

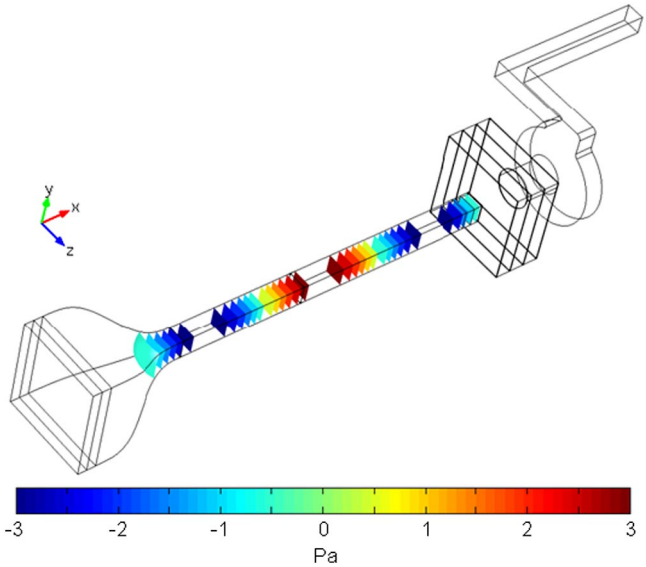

Fig. 8 Total acoustic pressure at 126.1 Hz excitation.

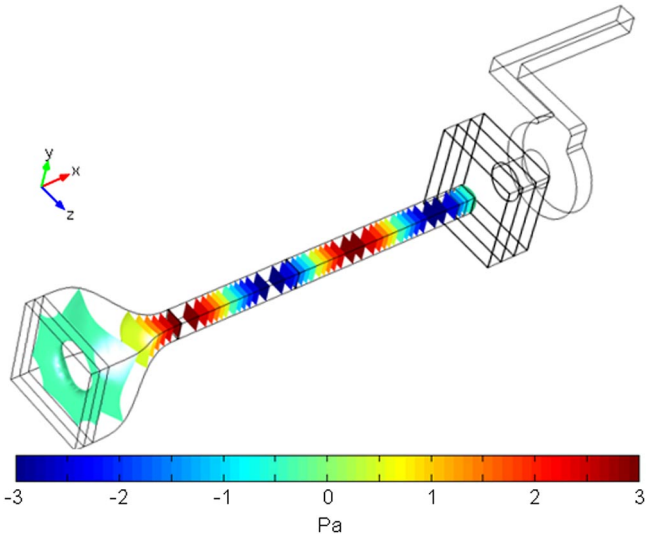

Fig. 9 Total acoustic pressure at 167.8 Hz excitation.

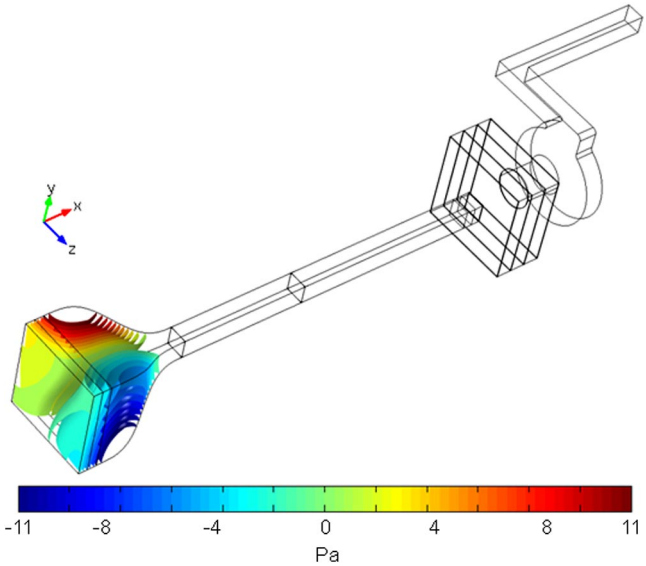

Fig. 10 Total acoustic pressure at 218.3 Hz excitation.

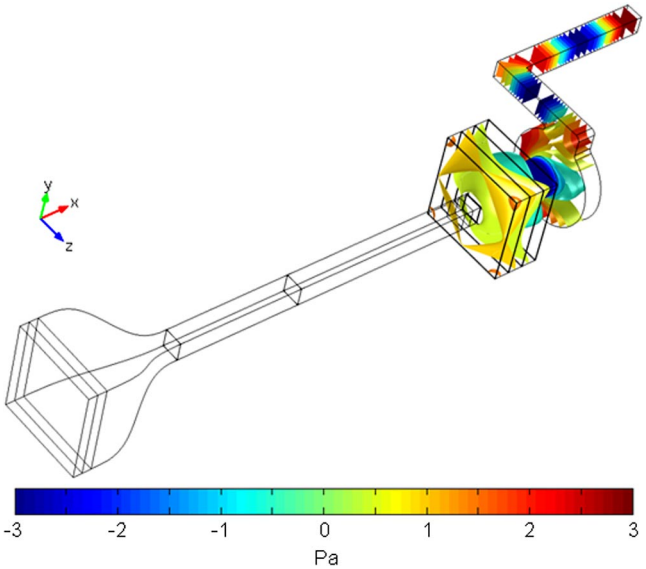

Fig. 11 Total acoustic pressure at 286.4 Hz excitation.

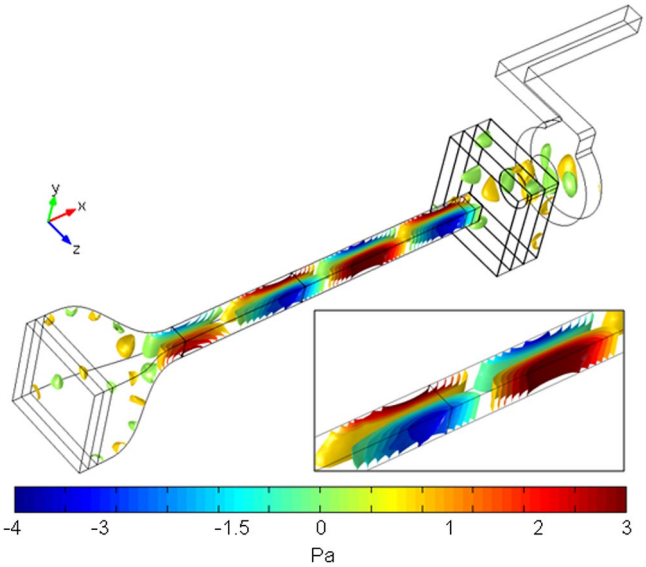

Fig. 12 Total acoustic pressure at 860.4 Hz excitation.

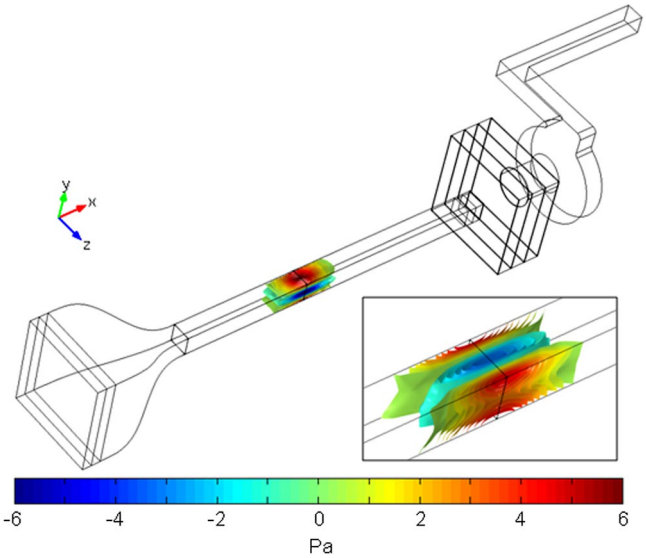

Fig. 13 Total acoustic pressure at 1715.1 Hz excitation.

In following, absent of the source terms, a dedicated eigenfrequency analysis is carried out to solve the eigenvalue problem of Eq. (19): $\lambda = i2\pi f = i\omega$ [40]. Visualization of the associated eigenmodes enables detection of the locations that host the resonance effect and distinguishes frequencies that entail local influence on the measurement surface.

IV. Results and Discussion

A. Numerical Acoustic Resonance Analysis

Initially, facility response to sound forcing in the 100–300 Hz frequency range is presented by TL in Fig. 7 by a 2 Hz computational frequency step. Apparent distinct peaks at 126, 168, 218, and 286 Hz are associated with a reduced transmission loss behavior as sound waves propagate through the channel. The first peak at 126 Hz is consistent with the longitudinal base harmonic that is analytically predicted by Eq. (13) (1.4 m mesh distance, 20°C air temperature) at 123 Hz.

The acoustic eigenmodes associated with the highlighted frequencies are illustrated by distributions of the total acoustic pressure in Figs. 8–11. Evidently, for 126 Hz, a standing wave occupies the straight duct section, and hence exerts a strong direct influence on the measurement surface (Fig. 8). Along these lines, the resonance mode at 168 Hz exhibits a coupled behavior containing the bell-mouth inlet as well as the duct section (Fig. 9). Similar to the case of 126 Hz excitation, the dominant effects occupy the test section.

On the contrary, while analyzing the total acoustic pressure trends for the 218 and 286 Hz resonances, a remarkably different mode shape pattern is observed (Figs. 10 and 11). The 218 Hz resonance pattern is clearly seen to be located in the bell-mouth inlet such that the strongest pressure fluctuations are confined to the area upstream of the test section. However, for the 286 Hz forcing, the excitation mode shape is limited to the far-downstream settling chamber and compressor casing. Therefore, these low transmission loss regions at higher frequencies are not relevant to investigations conducted in the straight channel test section.

Focusing on the transverse resonance modes, the total acoustic pressure distributions at 860 and 1715 Hz are presented in Figs. 12 and 13. These identified eigenfrequencies are in close agreement with the analytical fluid column model [Eq. (13)], which predicts transverse natural frequencies at 858 and 1716 Hz, respectively.

The eigenmode associated with 860 Hz is seen to be most indicative of a standing wave pattern, which suggests the coupled interaction of a transverse and a longitudinal resonance (Fig. 12). The mode shape inside the straight duct section clearly exhibits two and four sound pressure antinodes in the widthwise and streamwise directions, respectively. Considering the effective straight duct length of 3.26 m, using Eq. (13), the frequency that corresponds to a longitudinal fourth harmonic resonance response mode equals 214.7 Hz, as seen in Fig. 12. This value coincides with the fourth subharmonic of the 860 Hz excitation frequency. Accordingly, the imposed forcing frequency overlaps with the transverse base harmonic response, indicated by two widthwise pressure antinodes located at the tunnel sidewalls. For both cases of longitudinal and transverse resonances, the corresponding antinodes are seen to oscillate temporally out of phase.

In the case of 1715 Hz excitation (second transverse harmonic), a characteristic resonance pattern located roughly in the center of the channel exhibits three pressure antinodes in the transverse direction. Contrary to 858 Hz forcing, no coupling between longitudinal and transverse eigenmodes is observed. In light of these results, the acoustic impact of 858 and 1716 Hz excitations on the measurement location flowfield are expected to be notably distinct from one another.

B. Experimental Heat Transfer Investigation

To investigate the heat transfer ramifications of complex standing sound wave patterns, liquid crystal thermometry measurements are conducted on a flat plate at a constant mean channel Reynolds number of $Re_D = 56{,}800$. Based on the prior numerical acoustic analysis, the channel is subjected to 858 and 1716 Hz excitations at a SPL of 120 dB. In addition, highlighting the role of resonances, a reference investigation is conducted at the 8560 Hz high-frequency forcing, where the channel is only subjected to traveling waves. The speaker is mounted in the wall-normal direction, perpendicular to the TLC surface (Fig. 3). The measurement surface comprises a 12×18 cm rectangular area, situated a 0.7 m distance from the upstream inlet.

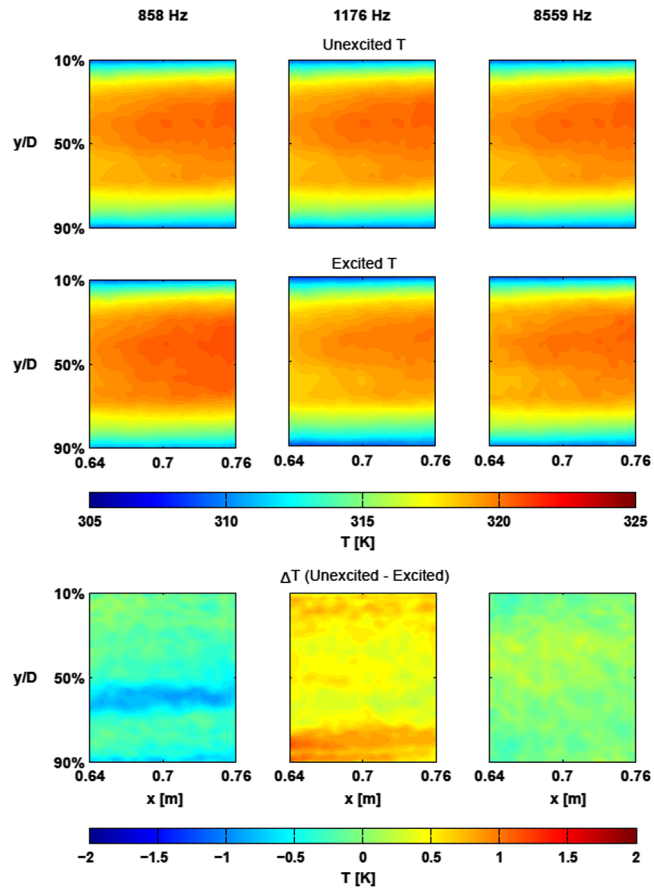

Fig. 14 Surface temperature distributions: (top) unexcited, (middle) acoustically excited, (c) differential change due to excitation.

To ensure accurate quantification of the unexcited baseline condition and to further verify the repeatability of surface temperature measurements, the reference case absent of forcing is acquired before and after each measurement. Between two image acquisitions, sufficient time (30 min) is provided to compensate for the thermal inertia and to allow steady-state conditions for every measurement. Throughout the total experimentation duration of 3.5 h, the periodically monitored ambient air temperature remains constant within ± 0.2 K. Therefore, for consistency, the baseline case unexcited surface temperatures of all four acquired steady-state instances are averaged; deviation from the mean among these reference cases is observed to be less than ± 0.25 K. Characterizing the uncertainty of ΔT, the wall temperature precision error is calculated to be on the order of ± 0.3 K in the 95%-confidence interval.

Figure 14 presents characteristic surface temperatures in the absence and presence of sound excitation at 858, 1716, and 8560 Hz. To highlight the forcing-induced changes in local temperature, the findings are also charted in terms of $\Delta T = (T_{\text{Unexcited}} - T_{\text{Excited}})$. Analyzing the findings for the 858 Hz excitation case, in reference to the unexcited distribution, a slight increase in surface temperature (1 deg order) is observed to be concentrated around the horizontal centerline, whereas regions toward the passage lateral wall appear less affected. Opposing this trend, distributions subjected to the 1716 Hz forcing exhibit a clear global reduction in surface temperatures of $\sim$1.5 deg. The lowered temperature regions appear to be concentrated in three distinct horizontal streaks, manifesting itself weakly in the center and more prominently toward the two passage

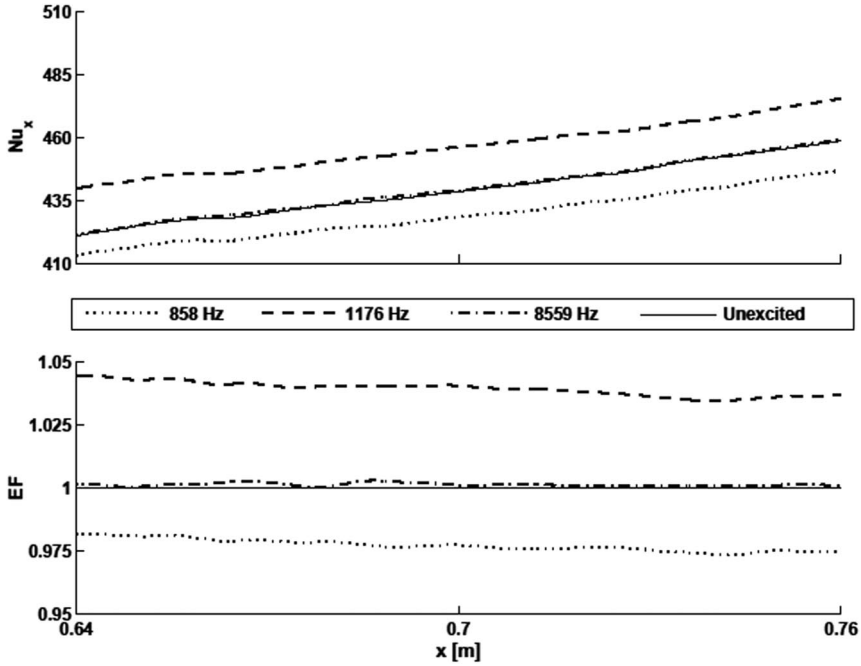

Fig. 15 Surface Nusselt number and enhancement factor.

sidewalls. For the 8560 Hz excitation, evidenced by the contours within 0.28 K, there appears to be no evident change in surface temperature.

Subsequently, the resultant changes in convective heat transfer are studied by characterization of the Nusselt number as well as the associated enhancement factor (Fig. 15). In the unexcited case, the laterally averaged Nu_x is computed to be 456 ± 19, which is within the value to the uniform surface flux heat transfer correlation [41] for turbulent flows:

$$Nu_x = 0.0308 \cdot Re_x^{4/5} \cdot Pr^{1/3} \tag{22}$$

Comparing the findings of different excitation frequencies, it becomes evident that, although 858 Hz results in a slight decrease in convective heat transfer, an increase ensures the 1716 Hz forcing. Consistent with the surface temperature trends, the 8560 Hz case does not appear to be conducive to any changes from the unexcited baseline condition. To illustrate the effects of excitation on turbulent boundary-layer heat transfer, the enhancement factor is computed. It is seen that 858, 1716, and 8560 Hz yield a 2.3% reduction, a 4% augmentation, and no change in local heat transfer, respectively. In contrast, the uncertainty of enhancement factor is estimated to be within $\pm 1.5\%$ in the 95%-confidence interval. In general, the findings reveal small but quantifiable differences in the sound-modified local heat transfer.

C. Discussion

Contrasting the predicted resonance modes by the eigenfrequency analysis with the experimental heat transfer findings, there appears to be some correlation with the excited resonance mode and the changes in local temperature distributions.

In the 858 Hz excitations, there exists the coupled interaction of a base transverse harmonic and a fourth longitudinal resonance (Fig. 12). Accordingly, the acoustically excited increase in surface temperature, situated around the horizontal centerline (Fig. 14), can be attributed to the concomitant local transverse sound pressure node (velocity antinode). This would imply a regional heat transfer reduction, which is likely associated with a dissipative entropy generation mechanism that locally augments the near-wall fluid temperature. The findings of the 1716 Hz forcing portray consistent phenomenological behavior, such that the three pressure antinodes (located at centerline, top, and bottom wall; Fig. 13) are seen to introduce a local reduction in surface temperature. Corroborating the prior observations, the 8560 Hz case merely induces a traveling wave excitation and, absent of a resonance behavior, no change in surface temperature or heat transfer is observed (Fig. 14). Moreover, in the presence of a standing wave, the net heat transfer alteration (Fig. 15) seems to inherit nonlinear characteristics (temporal and spatial), portraying a different influence based upon varying excitation conditions.

V. Conclusions

The design of a low-speed wind-tunnel facility, geared toward the investigation of sound-modified convective heat transfer, is presented in detail. A computational analysis of the characteristic acoustic resonance behavior is conducted by solving the Helmholtz equation in the frequency domain.

Acquired by the numerical model, the total acoustic pressure signature highlights that each component (including the bell mouth, duct section, honeycomb, mesh structures, settling chamber, and compressor casing) contributes to the constructive interference of varying-frequency incident pressure waves. Therefore, the acoustic resonance behavior of such experimental facilities should be analyzed in a comprehensive manner, such that the excitation frequencies employed throughout the investigation can be geared toward avoiding or matching various resonance modes. Hence, the geometrical shape of an experimental facility can be used to tailor the resulting natural frequencies to a desired acoustic response to controlled periodic forcing.

The possibility to excite resonance modes both in the transverse and longitudinal directions of the test section is demonstrated. Associated standing wave patterns, and arising pressure nodes and antinodes, are discussed in detail.

The convective heat transfer ramification of acoustic forcing is experimentally studied by means of steady wideband liquid crystal thermometry. The suitability of the experimental technique to the present application is clearly demonstrated. The general findings indicate that modification of turbulent flow convective heat transfer by conducive sound excitation is possible.

Based upon the varying excitation frequency and resonance mode, local regions of elevated and reduced surface temperatures are observed. Contrasting the findings with the numerically predicted standing wave patterns, sound pressure nodes, and antinodes are found to induce (to a varying degree) locally lower and higher rates of heat transfer, respectively. Globally, a consequent average heat transfer alteration is observed, and the net effect is similarly

dependent upon the excitation frequency. In contrast to standing waves, traveling waves are seen to be ineffective. Overall, although the acoustically induced changes are small in magnitude, the dependence on the excitation frequency is still quantifiable beyond the measurement error.

Acknowledgments

The authors acknowledge the financial support of Technion–Israel Institute of Technology, the Minerva Research Center (Max Planck Society contract AZ5746940764), the Israel Science Foundation (individual grant 1752/15), and the L. Kraus Research Fund toward initialization of this work. Furthermore, the scholarships that were used toward accommodation of Claudio Selcan in Israel, provided by Heinrich Hertz-Stiftung (Ministry of Innovation, Science and Research of North Rhine-Westphalia) and Erich Becker-Stiftung (Fraport AG), are greatly appreciated.

References

[1] Greenblatt, D., and Wygnanski, I. J., "The Control of Flow Separation by Periodic Excitation," *Progress in Aerospace Sciences*, Vol. 36, No. 7, 2000, pp. 487–545. doi:10.1016/S0376-0421(00)00008-7

[2] Mechel, F., and Schilz, W., "Untersuchungen zur Akustischen Beeinflussung der Strömungsgrenzschicht in Luft," *Acustica*, Vol. 14, No. 6, 1964, pp. 325–331.

[3] Ahuja, K. K., and Burrin, R. H., "Control of Flow Separation by Sound," AIAA Paper 1984-2298, 1984.

[4] Rice, E. J., and Zaman, K. B. M. Q., "Control of Shear Flows by Artificial Excitation," NASA TM-100201, 1987.

[5] Kearney, S. P., Jacobi, A. M., and Lucht, R. P., "An Experimental Investigations of Thermal Boundary Layer Structure and Heat Transfer in Oscillating Flows Using CARS Spectroscopy and Cold-Wire-Anemometry," Univ. of Illinois Rept. ACRC-TR-154, Champaign, IL, 1999.

[6] Bogdanoff, D. W., "A Study of the Mechanisms of Heat Transfer in Oscillating Flows," Dept. of Aerospace and Mechanical Sciences, Princeton Univ. TR-483-f, Princeton, NJ, 1967.

[7] Schlichting, H., *Boundary Layer Theory*, Verlag G. Braun, Karlsruhe, Germany, 1968, pp. 128–130.

[8] Stuart, J. T., "Unsteady Boundary Layers," *Laminar Boundary Layers*, Oxford Univ. Press, Oxford, 1963, pp. 348–350.

[9] Panton, R. L., *Incompressible Flow*, Wiley, Hoboken, NJ, 2005, pp. 227–229.

[10] Clamen, M., and Minton, P., "An Experimental Investigation of Flow in an Oscillating Pipe," *Journal of Fluid Mechanics*, Vol. 81, No. 3, 1977, pp. 421–431. doi:10.1017/S0022112077002146

[11] Despard, R. A., and Miller, J. A., "Separation in Oscillating Laminar Boundary Layer Flows," *Journal of Fluid Mechanics*, Vol. 47, No. 1, 1971, pp. 21–31. doi:10.1017/S0022112071000909

[12] Lighthill, M. J., "The Response of Laminar Skin Friction and Heat Transfer to Fluctuations in the Stream Velocity," *Proceedings of the Royal Society of London Series A: Mathematical and Physical Sciences*, Vol. 224, No. 1156, 1954, pp. 1–23. doi:10.1098/rspa.1954.0137

[13] Stuart, J. T., "Unsteady Boundary Layers," *Recent Research of Unsteady Boundary Layers*, edited by Eichelbrenner, E. A., Presses de l'Universite Laval, Quebec, Canada, 1971, pp. 1–46.

[14] Kay, J. M., and Nedderman, R. M., "Fluid Mechanics and Transfer Processes," Cambridge Univ. Press, New York, 1985, pp. 258–260.

[15] Fand, R. M., and Kaye, J., "Acoustic Streaming near a Heated Cylinder," *Journal of the Acoustical Society of America*, Vol. 32, No. 5, 1959, pp. 579–584. doi:10.1121/1.1908151

[16] Richardson, P. D., "Local Effects of Horizontal and Vertical Sound Fields on Natural Convection from a Horizontal Cylinder," *Journal of Sound and Vibration*, Vol. 10, No. 1, 1969, pp. 32–41. doi:10.1016/0022-460X(69)90127-8

[17] Mozurkewich, G., "Heat Transfer from a Cylinder in an Acoustic Standing Field," *Journal of the Acoustical Society of America*, Vol. 98, No. 4, 1995, pp. 2209–2216. doi:10.1121/1.413335

[18] Loh, B.-G., and Lee, D.-R., "Heat Transfer Characteristics of Acoustic Streaming by Longitudinal Ultrasonic Vibration," *Journal of Thermophysics and Heat Transfer*, Vol. 18, No. 1, 2004, pp. 94–99. doi:10.2514/1.9156

[19] Kaiping, P., "Unsteady Forced Convective Heat Transfer from a Hot Film in Non-Reversing and Reversing Shear Flow," *International Journal of Heat and Mass Transfer*, Vol. 26, No. 4, 1983, pp. 545–557. doi:10.1016/0017-9310(83)90006-6

[20] Fujita, N., and Tsubouchi, T., "An Experimental Study of Unsteady Heat Transfer from a Flat Plate to an Oscillating Air Flow," *Heat Transfer — Japanese Research*, Vol. 11, No. 3, 1982, pp. 31–43.

[21] Cooper, P. I., Sheridan, J. C., and Flood, G. J., "The Effects of Sound on Forced Convection Over a Flat Plate," *International Journal of Heat and Fluid Flow*, Vol. 7, No. 1, 1986, pp. 61–68. doi:10.1016/0142-727X(86)90044-5

[22] Komarov, S., and Hirasawa, M., "Enhancement of Gas Phase Heat Transfer by Acoustic Excitation," *Ultrasonics*, Vol. 41, No. 4, 2003, pp. 289–293. doi:10.1016/S0041-624X(02)00454-7

[23] Feiler, C. E., "Experimental Heat Transfer and Boundary Layer Behavior with 100-CPS Oscillations," NASA TN-2531, 1964.

[24] Park, J. S., Taylor, M. F., and McEligot, D. M., "Heat Transfer to Pulsating Turbulent Gas Flow," *Proceedings of the Seventh International Heat Transfer Conference*, edited by Grigull, U., Hahne, E., Stephan, K., and Straub, J., Vol. 3, Hemisphere Publ. Corp., Washington, D.C., Sept. 1982, pp. 105–110.

[25] Purdy, K. R., Jackson, T. W., and Gorton, C. W., "Viscous Fluid Flow under the Influence of a Resonant Acoustic Field," *Journal of Heat Transfer*, Vol. 86, No. 1, 1964, pp. 97–106. doi:10.1115/1.3687082

[26] Purdy, K. R., Jackson, T. W., Willoughby, D. A., Keith, H. G., and Willbanks, C. E., "The Effect of a Resonant Acoustic Field on Laminar Flow in a Circular Tube," Georgia Inst. of Technology Rept. ARL65-96, Atlanta, 1965.

[27] Jackson, T. W., Purdy, K. R., Keith, H. G., and Rudland, R. S., "Investigations of the Effect of Acoustic Vibrations on Convective Heat Transfer," Georgia Inst. of Technology Rept. ARL-65-97, Atlanta, 1965.

[28] Jackson, T. W., Oliver, C. C., and Eastwood, I., "The Effects of Resonant Vibrations on Heat Transfer at High Reynolds Numbers," Georgia Inst. of Technology Final Rept. UCRL-13016, Atlanta, Aug. 1961.

[29] Jackson, T. W., Harrison, W. B., and Boteler, W. C., "Free Convection, Forced Convection, and Acoustic Vibrations in a Constant Temperature Vertical Tube," *Journal of Heat Transfer*, Vol. 81, No. 1, 1959, pp. 68–74.

[30] Lemich, R., and Hwu, C. K., "The Effect of Acoustic Vibration on Forced Convective Heat Transfer," *AIChE Journal*, Vol. 7, No. 1, 1961, pp. 102–106. doi:10.1002/(ISSN)1547-5905

[31] Gross, A. H., Osherov, A., and Gany, A., "Heat Transfer Amplification Due to Transverse Mode Oscillations," *Journal of Thermophysics and Heat Transfer*, Vol. 17, No. 4, 2003, pp. 521–525. doi:10.2514/2.6797

[32] Morse, P. M., and Ingard, K. U., *Theoretical Acoustics*, Princeton Univ. Press, Princeton, NJ, 1968, pp. 466–468.

[33] Bell, J. H., and Mehta, R. D., "Boundary-Layer Predictions for Small Low-Speed Contractions," *AIAA Journal*, Vol. 27, No. 3, 1988, pp. 372–374. doi:10.2514/3.10122

[34] Bell, J. H., and Mehta, R. D., "Contraction Design for Small Low-Speed Wind Tunnels," NASA TR-89, Aug. 1988.

[35] Brassard, D., and Ferchichi, M., "Transformation of a Polynomial for a Contraction Wall Profile," *Journal of Fluids Engineering*, Vol. 127, No. 1, 2005, pp. 183–185. doi:10.1115/1.1852492

[36] Thwaites, B., "Approximate Calculation of the Laminar Boundary Layer," *Aeronautical Quarterly*, Vol. 1, Nov. 1949, pp. 245–280.

[37] Cukurel, B., Selcan, C., and Arts, T., "Color Theory Perception of Steady Wide Band Liquid Crystal Thermometry," *Experimental Thermal and Fluid Science*, Vol. 39, May 2012, pp. 112–122. doi:10.1016/j.expthermflusci.2012.01.015

[38] Kline, S. J., and McClintock, F. A., "Describing Uncertainties in Single Sample Experiments," *Mechanical Engineering*, Vol. 75, No. 1, 1953, pp. 3–8.

[39] Bauer, A. B., "Impedance Theory and Measurements on a Porous Acoustic Liner," *Journal of Aircraft*, Vol. 14, No. 8, 1977, pp. 720–728. doi:10.2514/3.58844

[40] Crocker, M. J., "Handbook of Acoustics," Wiley/IEEE, New York, 2008, pp. 20–22.

[41] Incropera, F. P., and DeWitt, D. P., *Fundamentals of Heat and Mass Transfer*, Wiley, New York, 2002, pp. 397–399.